BULLETIN OF THE POLISH ACADEMY OF SCIENCES
TECHNICAL SCIENCES, Vol. 72(6), 2024, Article number: e151375
DOI: 10.24425/bpasts.2024.151375

Cascade-free predictive adhesion control for IPMSM-driven electric trains

Jiao REN[1] **and Ruiqi LI**[2]*

[1] Urban Vocational College of Sichuan,Chengdu 610031, China
[2] School of Electrical Engineering, Southwest Jiaotong University, Chengdu 610031, China

Abstract. The application of active adhesion control to the traction control system of an electric train holds great appeal for maximizing longitudinal acceleration force. Most of the currently reported works regulate the adhesion between wheel and rail by adjusting the torque reference of a cascade motor drive controller, which suffers from slow speed response and excessive start torque. This article proposes a cascade-free predictive adhesion control strategy for electric trains powered by an interior permanent magnet synchronous motor (IPMSM) to address these issues. The proposed control scheme utilizes an improved perturbation and observation method to predict the time-varying wheel-rail adhesion state and determine the optimal slip speed. The initial setpoint reference command from the driver master is then adjusted to a dynamic reference that continuously adapts to the predicted adhesion conditions. Finally, the predictive speed control method is employed to ensure rapid convergence of the tracking objective. The simulation and hardware-in-the-loop testing results confirm that this approach achieves excellent dynamic performance, particularly during the train start-up phase and in the high-speed weak magnetic area of the IPMSM.

Keywords: adhesion control; cascade-free; maximize longitudinal acceleration force; perturbation and observation; predictive speed control

1. INTRODUCTION

The acceleration and braking of a train rely on adhesion, which is the tangential force at the wheel-rail contact point in the direction of train movement. When the driving or braking force of the train exceeds the adhesion during acceleration or deceleration, the wheel slips in case the train is still running and slides in case braking occurs [1, 2]. To ensure the desired traction or braking force, adhesion control between the wheel and the rail has been developed. The primary objective of adhesion control is to prevent the wheel slip and maintain the adhesion under specific axle load and environmental conditions [3, 4]. The demand for high-speed and efficient trains has sparked a growing interest in the advanced functional objectives, namely, maximizing the utilization of adhesion while ensuring safety and comfort [5, 6].

In most studies on adhesion control, determining the reference slip and current adhesion condition is crucial. In [7], the reference slip is determined through pre-testing on the track. However, this method has limitations due to uncertainties in external weather and wheel-rail conditions. Therefore, [8] and [9] estimate the reference slip online using intelligent algorithms based on train operating parameters such as environment, speed, and slip ratio. Recently, an event-based adhesion control strategy has been proposed, which operates without relying on various parameters of train operation [10]. The state observers are commonly employed for adhesion state estimation as they can directly estimate the train adhesion coefficient. However, the state observer methods are sensitive to noise and variations in system parameters, which affect their accuracy. To improve the accuracy of adhesion estimation, the unscented Kalman filter is employed in [11, 12], which has shown promising results. Additionally, using information such as noise, train acceleration, and jerk, the adhesion state can be indirectly estimated [13, 14]. Once the train's reference slip and the adhesion state are determined, effective control methods can be employed in the design of adhesion controllers, such as sliding mode control, extremum-seeking control, and fuzzy control [15–17], among others. For the convenience of verifying adhesion control algorithms, a reduced-scale roller rig that simulates the train track and wheels has been developed [18].

It is worth noting that all these aforementioned adhesion controllers can be categorized as torque correction controllers, which are cascaded onto the traction control system, as shown in Fig. 1. In manual mode, the torque correction controller directly adjusts the torque command from the operating handle to maintain adhesion between the wheel and the rail. Similarly, in automatic mode, the torque reference is also regulated by the adhesion control, even though this control target is issued by the traction motor speed control loop automatically. The torque correction-based adhesion controller adapts well to both driving modes of the train by suppressing or promoting the output torque of the traction motor. However, the motor controller cascaded with the torque correction controller is generally driven by field-oriented control (FOC) or direct torque control (DTC) [19, 20]. These types of motor controllers are characterized by the utilization of a cascade structure, employing linear and relatively slow speed controllers, along with inner loops for current, torque, and flux control [21, 22]. Due to the cascaded nature of adhesion control and motor control, the higher starting torque provided by the speed controller in the initial phase is difficult to correct in

*e-mail: liricky@my.swjtu.edu.cn

Manuscript submitted 2023-11-08, revised 2024-07-03, initially accepted for publication 2024-07-13, published in November 2024.

the first instance by the torque correction adhesion controller, making the train susceptible to slippage during this phase. In addition, during certain special operation stages, such as sudden changes in track conditions and high-speed zones, the cascaded traction control architecture hinders further improvement in the overall adhesion utilization of the train. Moreover, the torque correction controller frequently adjusts the motor reference torque based on the time-varying adhesion state, resulting in an increase in torque harmonic content.

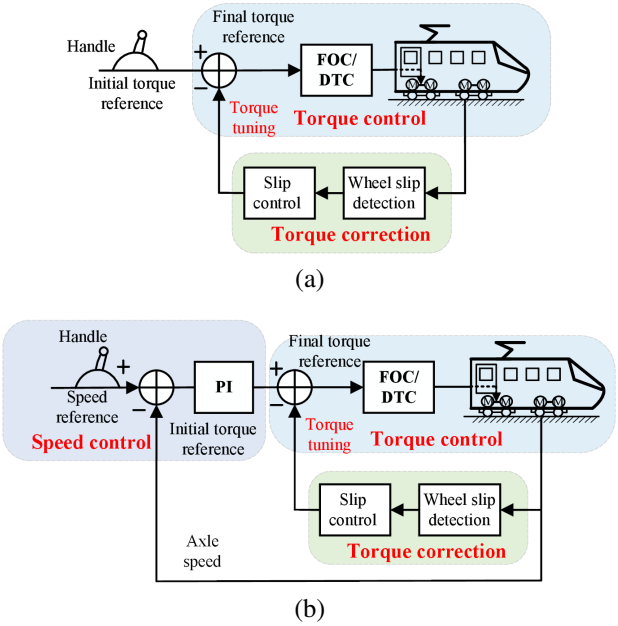

Fig. 1. Block diagram of a conventional torque correction-based adhesion control strategy: (a) manual mode; (b) automatic mode

To enhance control performance, several different motor control strategies have been proposed and implemented in electric traction systems. These strategies include model predictive control (MPC), active disturbance rejection control, and sliding mode control, among others [23–25]. Notably, a cascade-free predictive speed control strategy is introduced for electric trains, demonstrating exceptional dynamic performance [22]. However, these efforts have overlooked the adhesion dynamics between the train and the rail. In other words, the adaptability between the wheel-track adhesion controller and the motor drive controller has not been taken into account.

This paper presents a novel cascade-free adhesion control framework aimed at maximizing adhesion during the acceleration mode of electric trains. The framework integrates two control objectives: wheel-rail active adhesion control and speed regulation, into a dynamic reference tracking problem based on the predictive optimum adhesion state. An improved perturbation and observation (P&O) algorithm is employed to determine the time-varying reference. Subsequently, predictive speed control is utilized, which uses a single optimization algorithm to generate the control action for the next sampling instant, ensuring consistent operation of the train in the optimal slip state throughout the acceleration process. The innovations and contributions of this paper can be summarized as follows:

1. A cascade-free framework for adhesion control is proposed. This control topology represents a pioneering approach to slip control of electric train, which controls adhesion from the perspective of reference speed prediction and correction, rather than the regulation of reference torque.
2. In this cascade-free control framework, the P&O method in [8] is improved, endowing it with the ability to directly predict the electric train optimal slip speed. Besides, based on the predictive optimal slip speed, the initial static reference speed issued by the master controller is corrected to a dynamic reference that varies continuously with the adhesion conditions. Therefore, by tracking this time-varying speed control objective during the train speed regulation phase, the maximum longitudinal acceleration force can be achieved without the need for an additional adhesion controller.

The paper is organized as follows. In Section 2, the adhesion characteristics and the dynamic model of the train and the control objectives are described. Section 3 develops the cascade-free predictive adhesion control method. Section 4 presents the simulation and hardware-in-the-loop (HIL) platform test results. Finally, Section 5 concludes the article.

2. PROBLEM FORMULATION

2.1. Adhesion characteristics

The power of the electric train is transmitted to the wheels through the traction transmission system, as shown in Fig. 2. When the wheel is subjected to the torque generated by the traction motor, a small sliding occurs on the contact surface between the wheel and the rail. This phenomenon is commonly referred to as creepage. Creepage generates adhesion traction, propelling the train forward. Simultaneously, due to the existence of the creep phenomenon, a velocity difference occurs between the rolling linear velocity of the moving wheels and the forward velocity, known as the creep velocity (also referred to as the slip speed). The creep ratio λ, defined as the ratio of the

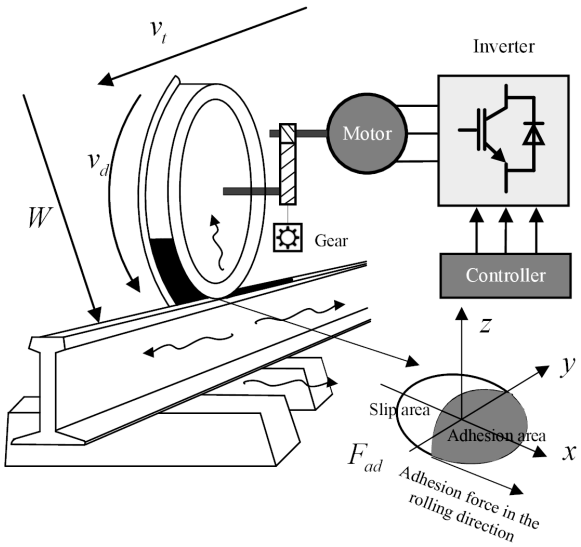

Fig. 2. Drive energy transfer path and wheel-rail contact model

creep velocity to the nominal velocity, characterizes the degree of creep [26, 27]. The creep rate can be expressed as:

$$\begin{aligned} \lambda &= \frac{v_s}{\max\{v_d, v_t\}}, \\ v_s &= v_d - v_t, \\ v_d &= w_d r_d, \end{aligned} \tag{1}$$

where v_s, v_d, v_t are, respectively, the train slip speed, the train wheel linear velocity, and the train body speed; r_d is the wheel radius; w_d is the axle speed of the wheel pair. Numerous tests have proven a close relationship between the adhesion characteristics and creep ratio, which is often described by the adhesion coefficient curve $\mu(\lambda)$ shown in Fig. 3. As shown in Fig. 3, both creep ratio and rail surface conditions affect the variation of the adhesion coefficient. The definition of adhesion coefficient demonstrates that the adhesion force F_{ad} is proportional to μ when the load is constant:

$$\mu(\lambda) = \frac{F_{\text{ad}}}{W}, \tag{2}$$

where W is the normal force of the motor car single axle. According to this definition, we can adjust the instantaneous adhesion coefficient of the train to make high use of the tangential force F_{ad}.

2.2. Dynamic model of electric train

Establishing an electromechanical coupling model of the electric train that can capture the relationship between electric control and adhesion characteristics is essential to build the control strategy from the electric control perspective. To provide a concise illustration of the designed controller, the analysis focuses on a simplified one-dimensional single-axle model of the train, neglecting various complex factors. And then we treat the one-dimensional single-axle model of the actual train as an equivalent rigid particle, and we treat the motion of the train as the motion of a rigid body, and this variable of the kinetic energy of the rigid body is equal to the work done by the external force. The adopted uniaxial train model satisfies the following force transfer equation [7]:

$$\begin{aligned} F_{\text{ad}} &= \mu(\lambda) W, \\ W &= m_w g, \\ J_w \frac{dw_d}{dt} &= T_w - F_{\text{ad}} r, \\ T_w &= T_e R_g, \\ T_l &= F_{\text{ad}} r / R_g \\ J_m \frac{dw_m}{dt} &= T_e - T_l - B_m w_m, \end{aligned} \tag{3}$$

where m_w is the total mass applied to single-axle; $m_w = \frac{m_M}{N_c}$; m_M is the total mass of a moving carriage; N_c is the number of traction units per rolling stock; g is the acceleration of gravity; R_g denotes the gear ratio of the gearbox; w_m is the rotor speed of the traction motor, $w_m = R_g w_d$; T_e, T_l are the electromagnetic torque and the equivalent load torque of the motor, respectively; J_m, J_w are the equivalent rotational inertia of the motor and the equivalent rotational inertia of the wheel pair, respectively; B_m is the viscous friction coefficient. As the IPMSM is used as the drive motor in this paper, the electromagnetic torque T_e can be expressed as

$$T_e = \frac{3p}{2}\left[(L_d - L_q) i_d i_q + \psi_f i_q\right], \tag{4}$$

where the stator current i_d and i_q satisfy the following voltage equation [28, 29]:

$$\begin{aligned} u_d &= R i_d + L_d \frac{d}{dt} i_d - L_q w_e i_q, \\ u_q &= R i_q + L_q \frac{d}{dt} i_q + L_d w_e i_q + w_e \psi_f. \end{aligned} \tag{5}$$

In (4) and (5), subscript d and q stand for direct and quadrature axle; u and i are stator voltage and current; R and L are stator resistance and inductance; $w_e = p w_m$ is electric angular velocity; ψ_f is permanent magnet flux linkage; p is the number of pole pairs.

Empirically, a moving train generally contains 2–6 power axles. The single power axle model can be combined to comprehensively reflect the essential characteristics of the traction device comprehensively. According to Newton's second law, using the combined single-axle model, the equation of motion of the whole train can be written as

$$\sum_{i=1}^{N_c \times N_{mc}} F_{\text{ad}i} - F_R = M \frac{dv_t}{dt}, \tag{6}$$

where N_{mc} stands for the quantity of moving cars; $F_{\text{ad}i}$ denotes the adhesion force of the i-th traction unit; F_R is the total amount of running resistance on the train, including but not limited to frictional resistance, air resistance, etc.; M is the total mass of the train.

2.3. Tracking control objectives

In the automatic mode of electric trains, the primary objective of traction control is to achieve the tracking of the target speed v_{t_ref} of the train body. Because of 'creep', as long as the wheel linear speed v_d reaches the target speed v_{t_ref} without slipping, the control objective is considered completed.

We also seek to maximize longitudinal traction during the traction phase of the train. From Fig. 3 and equation (2), it can be observed that the maximum adhesion can be obtained when the train is operating at point (λ_m, μ_m). According to the definition of creep ratio (1), at the operating point (λ_m, μ_m), the wheel linear velocity v_d satisfies

$$v_d = \lambda_m \max\{v_d, v_t\} + v_t = v_{s\_\text{ref}} + v_t, \tag{7}$$

where v_{s_ref} is the optimal slip speed. Equation (7) indicates that the rail provides maximum longitudinal traction as long as the wheel rolling line speed v_d and the train body speed v_t always maintain a difference of v_{s_ref}.

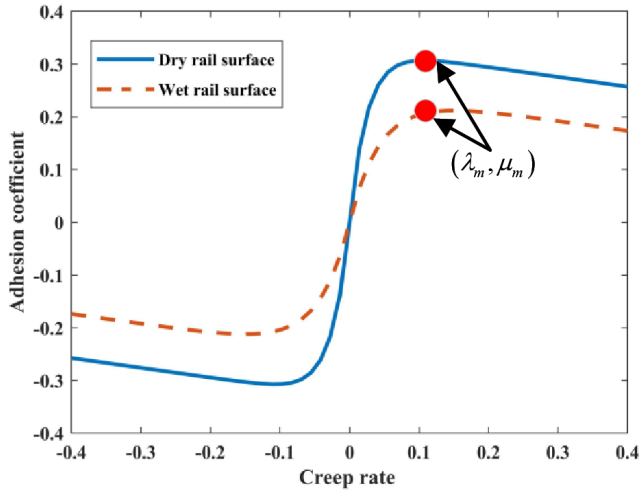

Fig. 3. Adhesion characteristics curve

In summary, this work aims to develop a control scheme for generating the control command u to fulfill the following control objectives:

1. Drive the electric train modeled by (3) and (6) to track the prespecified target speed trajectory v_{t_ref}.
2. Maintain the optimum slip speed v_{s_ref}.

In order to achieve both of these tracking control objectives, conventional methods employ separate designs shown in Fig. 1. Upon analyzing equation (7), it becomes evident that the time scales associated with these two control objectives (i.e., v_{t_ref} and v_{s_ref}) are inconsistent, with the first control objective exhibiting a significantly longer time scale compared to the second control objective. Therefore, below we consider the conversion of two tracking control objectives into one tracking control objective $v^*_{t\_\mathrm{ref}}$ in a dual-time-scale context.

3. CONTROL DESIGN

Figure 4 illustrates the block diagram of the developed cascade-free predictive adhesion control method. The proposed method

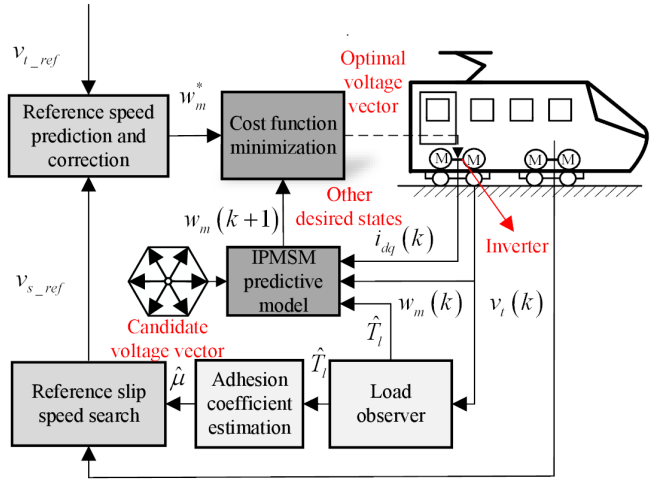

Fig. 4. General operation block diagram of the proposed cascade-free predictive adhesion control method

can be divided into three consecutive parts. Firstly, a load observer is designed to estimate the current adhesion state. Secondly, an improved P&O algorithm predicts the optimal slip and target speed online. Lastly, a predictive speed controller enables the train wheels to track the time-varying optimal reference speed rapidly. The detailed design of these three parts will be presented in the following subsections *A*, *B*, and *C*, respectively.

3.1. Adhesion coefficient estimation and motor speed prediction

Accurate motor load torque is needed to predict either the train adhesion state or the traction motor speed. The load torque can be estimated by taking the Laplace transform from (3) as given by [15]

$$\hat{T}_l = \frac{p_1}{s+p_1}\left(T_e - s\cdot J_m \cdot w_m\right), \tag{8}$$

where p_1 is the pole of the load torque observer.

Equations (2) and (3) state that the adhesion coefficient μ is proportional to the torque of the corresponding motor load, T_l. Therefore, the estimated value of the adhesion coefficient can be calculated by

$$\hat{\mu} = \frac{\dot{\hat{T}}_l R_g}{m_w g r}. \tag{9}$$

Similarly, the traction motor speed can be predicted with the help of a load torque observer. To obtain precise predictor variables, we discretize the mechanical equations of motion of the traction motor described in equation (3) using the modified forward Eulerian discretization formula

$$\begin{aligned} w^p_m(k+1) &= w_m(k) + T_s \cdot \frac{1}{J_m}\left(T_e(k) - \hat{T}_l\right), \\ w^s_m(k+1) &= w^p_m(k+1) + \frac{T_s}{2}\cdot\frac{1}{J_m}\Big[\left(T_e(k) - \hat{T}_l\right) \\ &\quad + \left(T^p_e(k+1) - \hat{T}_l\right)\Big], \end{aligned} \tag{10}$$

where T_s is the system sampling period; $w^p_m(k+1)$ is the predicted motor speed; and $w^s_m(k+1)$ denotes the corrected motor speed, which is also the final predicted motor speed. It is worth noting that the electromagnetic torque $T_e(k)$ can be calculated from equation (refeq4).

3.2. Best reference speed prediction

In the current train operation control system, the speed command v_{t_ref} of the train is issued by the commander controller. Subsequently, the train final operating speed is adjusted to a preset value through the action of the speed regulator. However, because of creep, an additional anti-slip controller is required to maintain the adhesion relationship between the wheels and the rails. In this section, we will present the approach for transforming the initial setpoint reference v_{t_ref} into an optimal dynamic tracking trajectory $v^*_{t\_\mathrm{ref}}$, with the aim of eliminating the design of the adhesion controller while achieving maximum adhesion control. The flowchart of the proposed method is illustrated in Fig. 6.

- Initially, compare the real-time wheel rolling speed v_d with the train body speed command v_{t_ref}. If the wheel speed v_d exceeds or is equal to the train body speed command v_{t_ref}, regardless of the adhesion control target, it indicates that the train is either in the cruise or braking phase. Since this article specifically addresses maximizing adhesion utilization during the train acceleration phase, there is no consideration for correcting the target speed v_{t_ref} at this stage. However, if the wheel speed v_d is slower than the train body speed command v_{t_ref}, it means that the train is in the traction phase. In this case, it is necessary to move the operating point toward (λ_m, μ_m) to achieve maximum acceleration, as depicted in Fig. 5.

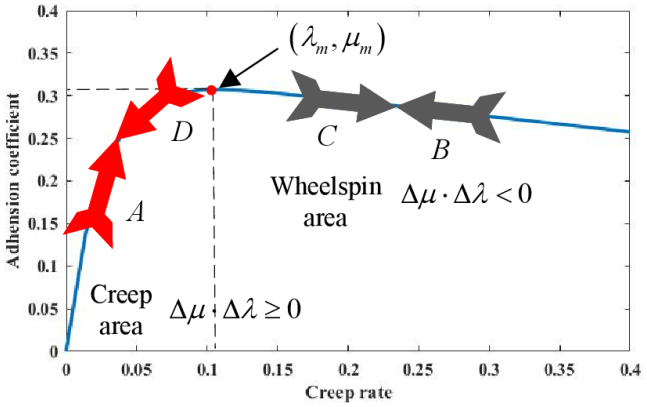

Fig. 5. Classification diagram of each operation point on the adhesion curve

- Secondly, determine the operating point owning the maximum adhesion coefficient [i.e., (λ_m, μ_m)]. By tracking the measured wheel slip and the estimated adhesion coefficient at each time step (i.e., $\lambda(k)$ and $\hat{\mu}(k)$ at time step k), the adhesion state of the train can be classified into four categories, namely A, B, C, and D, as shown in Fig. 5. However, due to uncertainties in system parameters, noise interference, and other factors, certain operating points may be erroneously categorized. Previous literature [30] has shown that changes in acceleration can also be used as criteria for determining the adhesion state. Because of this, introduce the train acceleration discriminatory criteria:

$$\begin{aligned} \Delta\hat{\mu} &= \Delta\hat{\mu}, \quad \Delta\hat{\mu} \cdot \Delta\alpha \geq 0, \\ \Delta\hat{\mu} &= 0, \quad \Delta\hat{\mu} \cdot \Delta\alpha < 0, \end{aligned} \tag{11}$$

where $\Delta\alpha$ is the ramp of the train acceleration, $\Delta\alpha = \alpha(k) - \alpha(k-1)$. Equation (11) shows that the estimated adhesion coefficient $\Delta\hat{\mu}$ is updated only when the estimated adhesion coefficient is consistent with the change in the ramp of the acceleration $\Delta\alpha$; Otherwise, the slope of the estimated adhesion coefficient is considered to be zero. The acceleration criterion will improve the discriminative accuracy of the estimated adhesion coefficient when the observer is stable. With the aid of estimated adhesion coefficient, we can determine the class to which the operating point belongs. For points belonging to classes A and D, the adhesion state satisfies $\Delta\hat{\mu}(k) \cdot \Delta\lambda(k) > 0$ where $\Delta\hat{\mu}(k) = \hat{\mu}(k) - \hat{\mu}(k-1)$, $\Delta\lambda(k) = \lambda(k) - \lambda(k-1)$. At this time, to move toward the point of (λ_m, μ_m), the operating point needs to move to the right side; for points corresponding to classes C and B, the adhesion state satisfies $\Delta\hat{\mu}(k) \cdot \Delta\lambda(k) < 0$, indicating that the operating end needs to move to the left side. Based on the above analysis, the updated formula of the reference creep slip state is designed as

$$\begin{aligned} &\eta = 1, \quad r = r_2, \quad \Delta\hat{\mu}(k) \cdot \Delta\lambda(k) > 0, \\ &\eta = -1, \quad r = r_1, \quad \Delta\hat{\mu}(k) \cdot \Delta\lambda(k) < 0, \\ &\eta = 0, \quad r = 0, \quad \Delta\hat{\mu}(k) \cdot \Delta\lambda(k) = 0, \end{aligned} \tag{12}$$

$$\lambda_{\mathrm{ref}}(k+1) = \lambda_{\mathrm{ref}}(k) + \eta \cdot r \cdot T_s, \tag{13}$$

where r is the adjustment rate and $\lambda_{\mathrm{ref}}(k+1)$ is the predicted optimum slip rate. Based on equation (12), the distance of each operation point from the point of (λ_m, μ_m) is evaluated. To be specific, for the operation point in the wheelspin area, the adjustment rate is set to $r = r_1$ $(r_1 > r_2)$ to achieve a faster update rate. On the other hand, for the operation point in the creep area, the regulation rate is set to $r = r_2$ to ensure a gradual approach towards the point (λ_m, μ_m) and avoid over-regulation. The continuous iteration of the adhesion state by equation (12) and equation (13) will make the operating point gradually approaches (λ_m, μ_m). $\lambda_{\text{allow-min}}$ and $\lambda_{\text{allow-max}}$ are the maximum and minimum allowable slip rates to ensure that the reference speed is within an acceptable range to avoid idling or skidding the locomotive. It is worth noting that the reference creep $\lambda_{\mathrm{ref}}(k+1)$ though iteration may not necessarily the optimum creep rate. For safety reasons, the reference creep rate $\lambda_{\mathrm{ref}}(k+1)$ obtained by iteration must be treated as follows.

1. *Case 1:* If the reference creep rate $\lambda_{\mathrm{ref}}(k+1)$ obtained from the iteration is less than or equal to the minimum allowable creep rate $\lambda_{\text{allow-min}}$, the minimum permissible creep rate $\lambda_{\text{allow-min}}$ is used as the reference creep rate for the next time step.
2. *Case 2:* If the reference creep rate $\lambda_{\mathrm{ref}}(k+1)$ obtained by the iteration is within the range of $(\lambda_{\text{allow-min}}|, \lambda_{\text{allow-max}})$, it is used as the reference creep rate for the next time step.
3. *Case 3:* If the reference creep rate $\lambda_{\mathrm{ref}}(k+1)$ obtained from the iteration is more than or equal to the maximum allowable creep rate $\lambda_{\text{allow-min}}$, the maximum permissible creep rate $\lambda_{\text{allow-max}}$ is used as the reference creep rate for the next time step.

After obtaining the reference creep rate $\lambda_{\mathrm{ref}}(k+1)$. From equation (1) and equation (13), one can obtain the real-time slip velocity as follows

$$v_{s\_\mathrm{ref}}(k+1) = \lambda_{\mathrm{ref}}(k+1) \cdot \max\{v_d, v_t\}. \tag{14}$$

- Finally, to ensure the rolling linear velocity of train's wheel and the real-time running speed of the train body during the

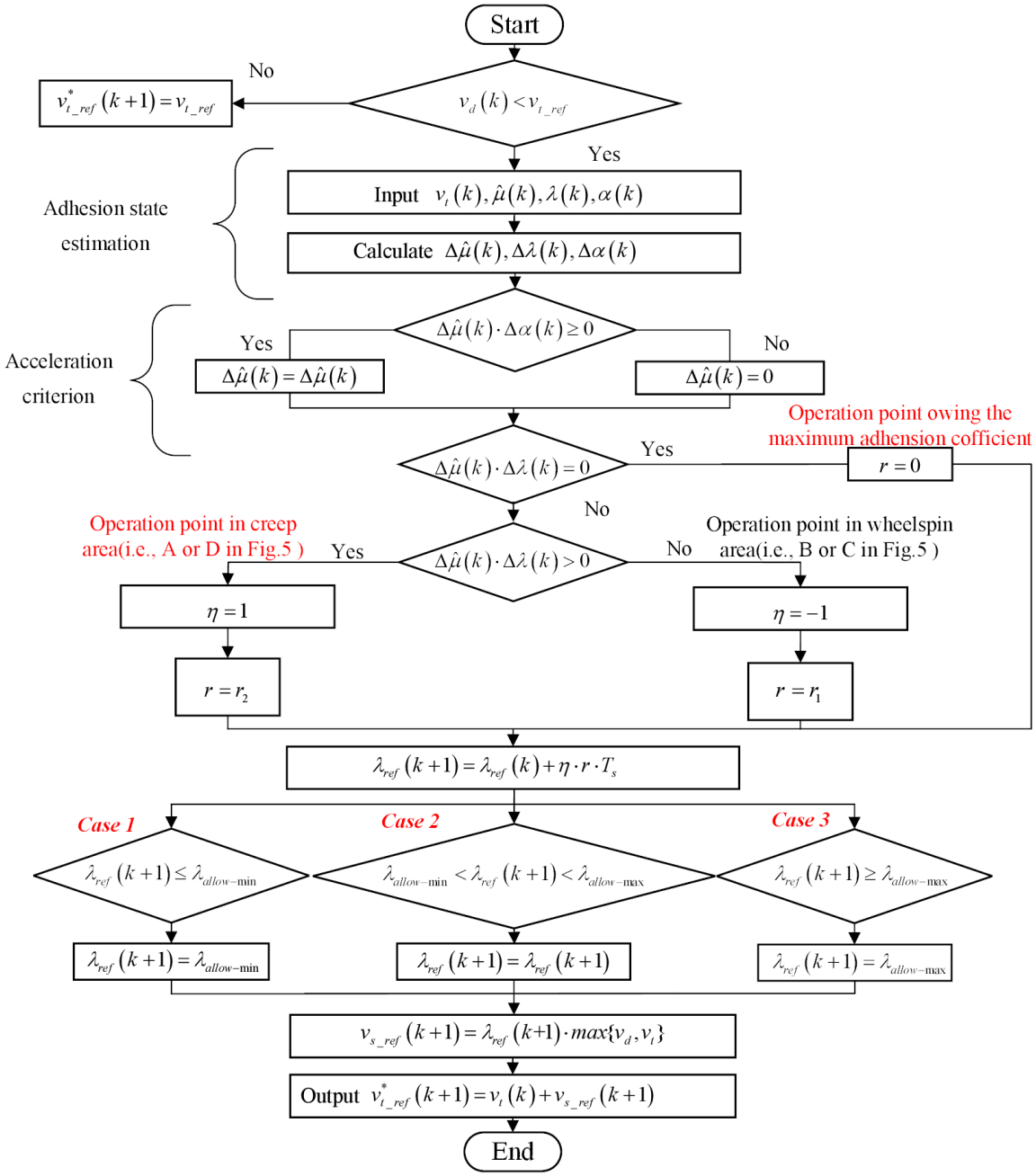

Fig. 6. Flowchart for predicting the optimal reference speed trajectory

traction phase always meet the requirements of the optimal reference slip speed, based on equation (1), equation (7) and equation (14), we correct the reference operating speed of the train v_{t_ref} to $v^*_{t\_\mathrm{ref}}$. The updated equation of $v^*_{t\_\mathrm{ref}}$ is

$$v^*_{t\_\mathrm{ref}}(k+1) = v_t(k) + v_{s\_\mathrm{ref}}(k+1), \tag{15}$$

where $v_t(k)$ is the train operating speed at time step k. It is worth pointing out that $v_t(k)$ should be $v_t(k+1)$ in real. Nevertheless, because of the high control frequency, $v_t(k)$ can be nearly equal to $v_t(k+1)$ within one sampling period. If equation (15) is directly input to the speed control system, the traction motor will not start. This is because, during the start-up phase, both the train body running speed and the slip speed are zero. To deal with it, a start term $\delta e^{-\beta t}$ is introduced, at which point the train will have an initial start speed. Moreover, the start term will decay to zero as the running time $t \to \infty$, without affecting the tracking of the optimal reference slip speed. The final reference speed of the train is

$$v^*_{t\_\mathrm{ref}}(k+1) = \delta e^{-\beta t} + v_t(k) + v_{s\_\mathrm{ref}}(k+1), \tag{16}$$

where δ is the initial start speed and β is the decay rate of the initial start speed. To avoid affecting the slip speed control, we set $\delta < 1$, $\beta > 1$.

The final reference speed (16) proposed in this paper depends on the instantaneous train body speed $v_t(k)$. Currently, the speed measurement method based on the train rolling linear velocity is the most commonly used train speed measurement method. However, as discussed in Section 2, the train rolling linear velocity is not equal to the actual train speed but rather an approximate value, due to the creep phenomenon. Therefore, to ensure the accuracy of the subsequently designed controller, more precise methods are desired to obtain the instantaneous train speed v_t with the correction of the train reference speed. Potential methods include radar speed measurement, satellite positioning, or multi-sensor fusion techniques [31–33].

3.3. Predictive speed control

The corrected reference speed is no longer a flat line but a curve that constantly varies with the operating speed and optimal creep ratio, as shown in Fig. 7. Once the real-time reference speed of the train, considering the optimal creep ratio, is obtained, it is converted to the equivalent motor reference speed

$$w_m^* = \frac{v_{t\_\mathrm{ref}}^*}{r_d} * R_g \,. \tag{17}$$

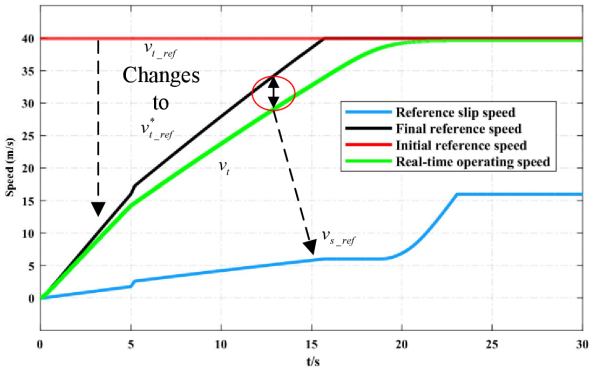

Fig. 7. Real-time reference velocity profile considering optimal creep ratio

Given that high-speed trains are a sizeable inertial system, the existing PI speed control algorithm used on trains faces challenges in quickly tracking the constantly changing reference speed profile with adhesion dynamics. The pre-experiments conducted on the experimental platform depicted in Fig. 8 found the predictive speed control algorithm advantageous in tracking fast time-varying references. Therefore, we will describe a predictive speed control algorithm in the following paragraphs. The speed prediction model (10) of IPMSM can be rewritten as

$$w_m(k+1) = w_m(k) + T_s f(T_e^p(k+1)) \tag{18}$$

where $f(T_e^p(k+1)) = \dfrac{1}{2\cdot J_m}[3(T_e(k) - \hat{T}_l) + (T_e^p(k+1) - \hat{T}_l)]$.

$T_e(k)$ can be calculated from the stator current at time step k

$$T_e(k) = \frac{3p}{2}\left[(L_d - L_q) i_d(k) i_q(k) + \psi_f i_q(k)\right]. \tag{19}$$

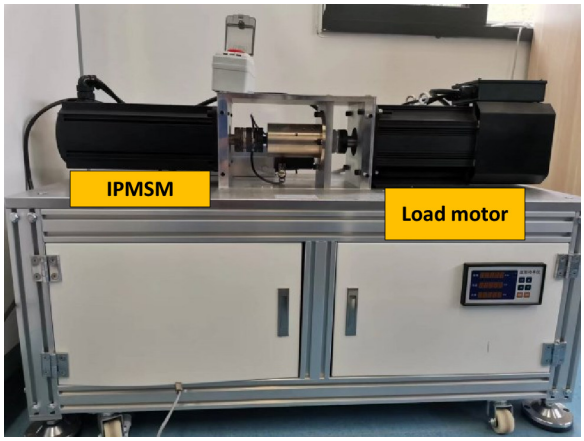

Fig. 8. IPMSM experimental platform

$T_e^p(k+1)$ can be calculated from the predicted stator current at time step $k+1$

$$T_e^p(k+1) = \frac{3p}{2}\Big[(L_d - L_q) i_d(k+1) i_q(k+1) + \psi_f i_q(k+1)\Big]. \tag{20}$$

The predicted stator current can be obtained by Eulerian discretization of the electric equation (5). Since the focus of this paper is not on the control of electric quantities, a detailed model of this process is not provided.

In this paper, the conventional two-level voltage source inverter is used as the motor driver. This type of inverter is capable of generating eight fundamental voltage vectors, denoted as $\boldsymbol{u} = (u_0, u_1 ..., u_7)$. Therefore, combining equations (4), (5), and (18), the motor speed can be predicted from the eight different voltage vectors at the moment $k+1$. Based on MPC theory, substituting the predicted eight motor speeds into the cost function (i.e., the square of the residual difference between the predicted motor speed and the predicted reference speed) separately, the voltage vector with the minimum cost function is selected as the optimal voltage vector for the k+1 time step and acted on by the traciton motor through the inverter.

$$F_c = \gamma_{w_m} \cdot \left(w_m^* - w_m(k+1)\right)^2 + F_{\mathrm{lump}}\,, \tag{21}$$

where γ_{w_m} is weighting factors; F_{lump} is a set sum function that weights the other desired electric states.

The first term in equation (21) evaluates the distance of each predicted motor speed from the desired reference speed. Note that when the weight γ_{w_m} is constant, the cost function of the speed error term will reduce, as the actual speed gradually approaches the reference speed. To improve the tracking accuracy of the controller with minor errors, a dynamic adjustment weight factor is introduced [34]

$$\gamma_{w_m} = k_1 e^{(k_2(1 - \frac{abs(w_m^* - w_m)}{w_{\max}}))} \tag{22}$$

where k_1, k_2 are the constant coefficients to adjust the weight, w_{max} is the maximum electric angular speed.

$$u^* = \underset{u_0,u_1,\ldots,u_7}{\arg\min} \left\{ \gamma_{w_m} \cdot \left(\frac{\delta e^{-\beta t} + v_t(k) + v_{s\_\mathrm{ref}}(k+1)}{r_d} \cdot R_g - w_m(k+1) \right)^2 + F_{\mathrm{lump}} \right\}, \tag{23}$$

F_{lump} is utilized to optimize the stator current and achieve good torque performance while ensuring the current remains within a safe amplitude range. Since these aspects are not the primary control objectives of this paper, they are not detailed here for brevity, and detailed design considerations can be found in Appendix.

Coupling (16), (17), (21) leads to the final predictive speed controller (23), shown at the top of next page.

In summary, the proposed control strategy achieves both speed regulation and adhesion control for the train by changing the initial reference speed without the need for additional adhesion control equipment. This approach avoids adjusting the creep ratio by torque correction, resulting in a higher accuracy of the creep rate (closer to the optimal creep ratio) and thus improved the utilization of the adhesion between the train wheels and rails.

4. SIMULATION AND HIL PLATFORM TEST RESULTS

4.1. Simulation conditions

At present, there are no public parameters of the electric multiple unit (EMU) driven by IPMSM. Therefore, CRH3's train body are used as simulation train model parameters shown in Table 1 [35]. A IPMSM for a certain type of 160 km/h power-concentrated EMU (FXD1-J) is selected as the prototype motor for simulation shown in Table 2. The running resistance of the train is given as

$$F_R = 6.796 + 0.0062 v_t + 0.000143 v_t^2 . \tag{24}$$

Empirically, the adhesion characteristic curves of different railway conditions can be approximated in the following way [27, 36]

$$\mu(\lambda) = \begin{cases} a(1 - e^{-b\lambda}) - \dfrac{\lambda}{c}, & \text{if } \lambda \geq 0, \\ -a(1 - e^{b\lambda}) - \dfrac{\lambda}{c}, & \text{if } \lambda < 0. \end{cases} \tag{25}$$

Based on an empirical formula, two railway conditions are set for the train operation. i.e., a dry railway condition for the first 10 s and a wet railway condition after 10 s. The coefficients for different railway conditions are given in Table 2. For dry rail surfaces, the optimal adhesion operation point (λ_m, μ_m) is (0.107, 0.3072). For wet rail surfaces, the optimal adhesion operation point is (0.155, 0.2116).

The parameters of the proposed control strategy are shown in Table 3. The target rolling linear velocity of the train in this paper is 28.68 m/s, equivalent to a traction motor speed of 1500 r/min.

Table 1
Electric train traction system parameters

Parameter	Value
Vehicle weight(t)	$M = 61.8$
Axle weight(t)	$m_w = 15.45$
Wheel radius(m)	$r = 0.43$
Gear ratio	$R_g = 2.355$
Wheel moment of inertia (kg.m^2)	$J_w = 100$
Motor rotational inertia (kg.m^2)	$J_m = 16$
Number of traction units	$N_c = 2$
Number of IPMSM pole pairs	8
IPMSM rated power (kW)	1225
IPMSM rated voltage (V)	1660
IPMSM rated current (A)	477
Maximum starting current (A)	680

Table 2
Rail surface parameters

Rail surface conditions	a	b	c
Dry rail surface	0.3315	40.19	5.392
Wet rail surface	0.2478	22.87	5.396

Table 3
Control system parameters

Parameters	Value	Parameters	Value
β	0.01	$\lambda_{\text{alllow-min}}$	0.04
r_1	1	$\lambda_{\text{alllow-max}}$	0.4
r_2	0.2	k_1	1 500 000
δ	−15	k_2	10
$T_s(s)$	1×10^{-5}	$w_{\max}$ (rad/s)	261

4.2. Simulation results

Figure 9 shows the control performance of the train body speed and rolling linear velocity. Firstly, it can be seen that the initial reference speed of the train undergoes a change from a straight line to a slowly rising smooth line after the prediction correction. Consequently, with the proposed control method, the train wheels steadily track the corrected reference speed within the first 19 s. Figure 12 shows the tracking performance for the creep ratio. At 18.42 s, the actual creep ratio between the wheel and the rail is measured to be 0.15, with an error of only 0.005 compared to the optimum creep rate. It is found that the proposed method can accurately predict and track the optimal slip velocity for various rail conditions, even when the wheel-rail situation abruptly transitions from dry to wet at 10 s.

Further, this indicates that during this phase, the train exerts maximum traction and operates at maximum acceleration. However, after 19 s, the rolling linear velocity speed wheel starts to

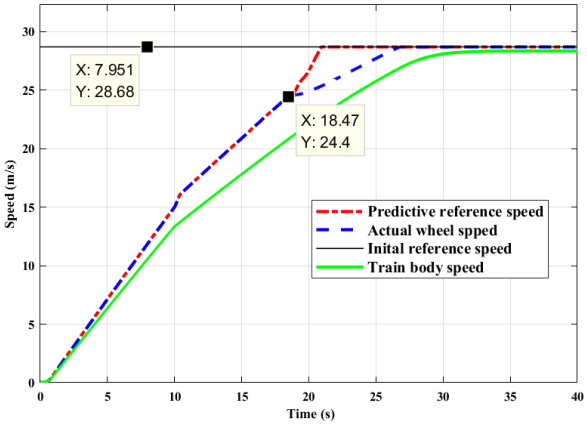

Fig. 9. Wheel and train body speed tracking performance

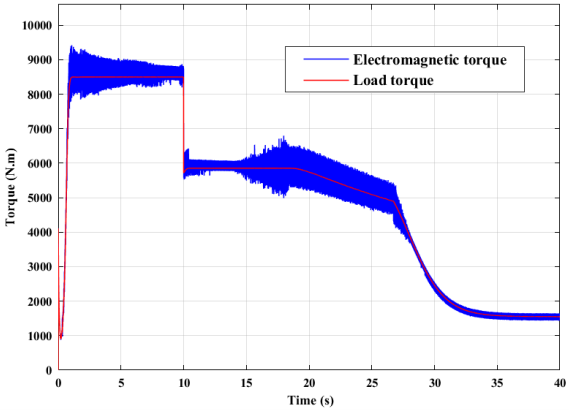

Fig. 11. IPMSM electromagnetic torque and load torque performance

gradually deviate from the reference speed, eventually reaching the preset value at 27 seconds. Throughout this phase , the acceleration continues to decrease, and the improved P&O algorithm starts to deviate from the actual optimal creep rate.

It can also be observed that the acceleration drops after 19 s, i.e., the shaft speed does not track to the predicted optimum speed, can be explained by the voltage constraint equation (equation (26)), where $\sqrt{(Ri_d - w_e L_q i_q)^2 + (Ri_1 + w_e L_d i_d + w_e \psi_f)^2}$ represents the stator voltage and $u_{\max}$ means the maximum inverter output voltage. When the motor speed exceeds the baseline speed, the torque current decreases due to the constraint imposed by the maximum output voltage $u_{\max}$ of the inverter. The IPMSM runs from the constant torque zone to the weak magnetic area. The IPMSM cannot provide enough electromagnetic torque to maintain maximum adhesion traction, as shown in Fig. 10 and Fig. 11.

$$\sqrt{(Ri_d - w_e L_q i_q)^2 + (Ri_1 + w_e L_d i_d + w_e \psi_f)^2} \le u_{\max}\,. \quad (26)$$

To further validate the control performance of the proposed method, we conducted a comparison with a PI torque correction-based technique. The parameters of PI torque correction-based controller are $Kp = 1000$, $Ki = 0.1$. These were tuned using a trial-and-error method based on engineering experience. At present, the specific parameter adjustment methods in PI-based adhesion lack control. Without loss of the generality, the torque correction method also uses an improved P&O strategy to predict the adhesion state between the wheels and the rails. The motor control algorithm in the torque correction method consists of a PI control for the outer loop and model predictive current control combined with maximum torque to current ratio control for the inner loop. The following evaluation function was employed to evaluate the adhesion performance of the train during the acceleration phase.

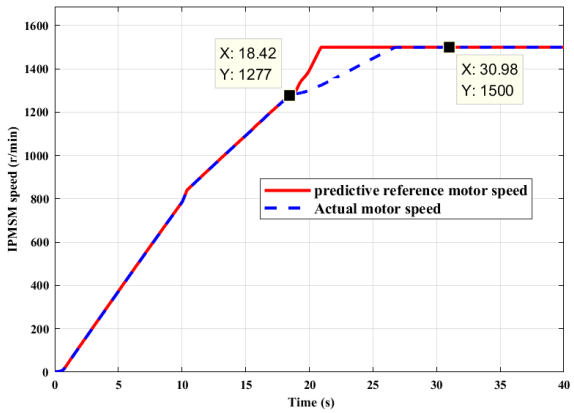

Fig. 10. IPMSM speed tracking performance

$$\eta_{\text{ad}} = \frac{\mu_{\text{ave}}}{\mu_{\text{opt-ave}}} = \frac{\int_0^{t_{\text{acc}}} \mu \, \mathrm{d}t}{\int_0^{t_{\text{on}}} \mu_{\text{opt}} \, \mathrm{d}t}\,, \quad (27)$$

where η_{ad} is the adhesion efficiency; μ_{ave} is the average adhesion coefficient during acceleration; $\mu_{\text{opt-ave}}$ is the average optimal adhesion coefficient available to the wheel-rail; and t_{acc} denotes the time taken by the train throughout the acceleration process.

The adhesion efficiency of the two methods calculated by (27) is given in Table 4. As seen in Table 4, the proposed method takes 32.58 s to reach the target speed, which is 7 s faster than the comparison method. The adhesion efficiency of the proposed method is 88.38%, indicating a 9.99% improvement compared to the torque-corrected process.

Table 4
Computational burden overview

Parameters	PI method	Proposed method
Execution time	27 µs	30 µs
Processor utilization	27%	30%

Figure 13 shows the control performance of the train body speed for both methods. In the early stage of the traction phase, the method based on torque correction exhibits faster speed. As the traction phase progresses, the proposed method gradually outpaces the torque correction-based method, reaching the preset speed 7 s earlier. From the control performance of the vehicle

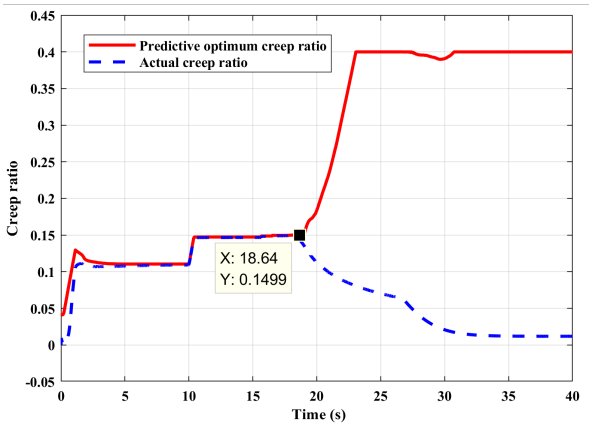

Fig. 12. Creep ratio performance

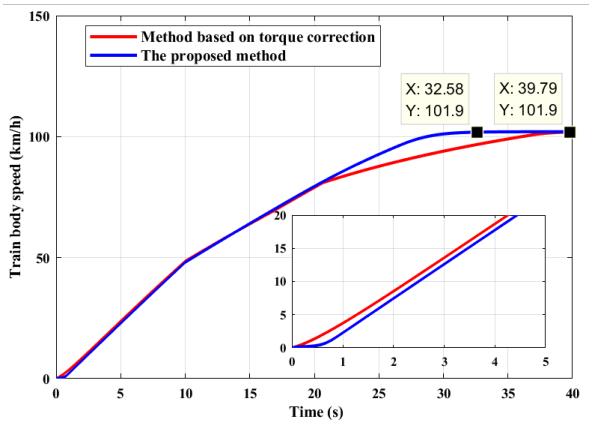

Fig. 13. Performance of train body speed with comparative simulation

acceleration (Fig. 14) and the coefficient of adhesion between wheels and rails (Fig. 15), it can be seen that the coefficient of adhesion and acceleration of the proposed control method consistently exceed those of the comparison method, except for the early stage of the traction phase (0–2 s). Particularly, after entering the weak magnetic zone, the train acceleration controlled by the proposed method decreases monotonically and smoothly.

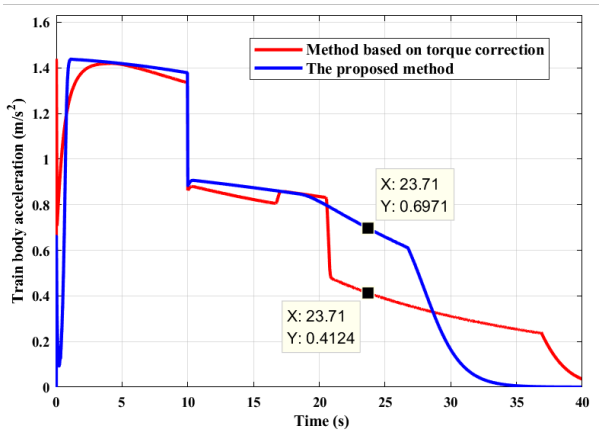

Fig. 14. Performance of train body acceleration with comparative simulation

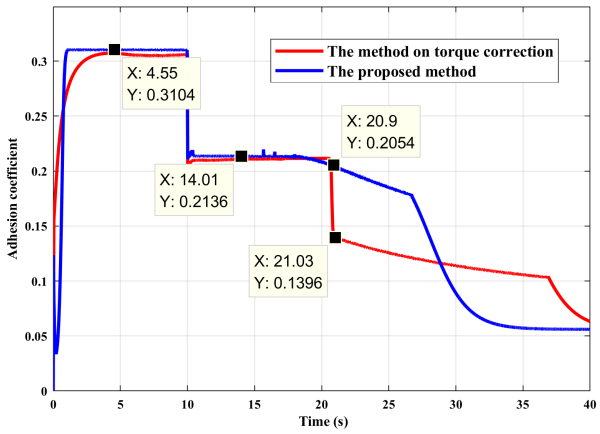

Fig. 15. Performance of train adhesion coefficient with comparative simulation

In contrast, the acceleration controlled by the torque correction method undergoes a sudden drop. The performance of the motor torque (Fig. 17) reveals the reason for the sudden drop in the acceleration of the train controlled by the torque correction method in the weak magnetic zone. When entering the soft magnetic area, the motor cannot generate enough torque to maintain an optimal sticking condition. The weakening of the adhesion state causes the torque correction to increase and the electromagnetic torque to decrease further, which in turn causes the adhesion coefficient and acceleration of the train to plummet.

Figure 16 shows the creep rate variation curve for the torque correction method. From 0–5 s, the actual creep rate of the train gradually moves from 1.0 (slip zone) to the predicted reference creep rate. The difference with the creep ratio control performance of the proposed method (Fig. 11) is that the actual creep ratio of the proposed method is always stable in the creep zone. In contrast, due to the ample initial start torque (Fig. 17), the torque correction method causes the actual initial creep ratio to operate in the slip zone before gradually approaching the optimum creep ratio. This behavior explains why the train is more prone to slipping during the start-up phase when using the torque correction method.

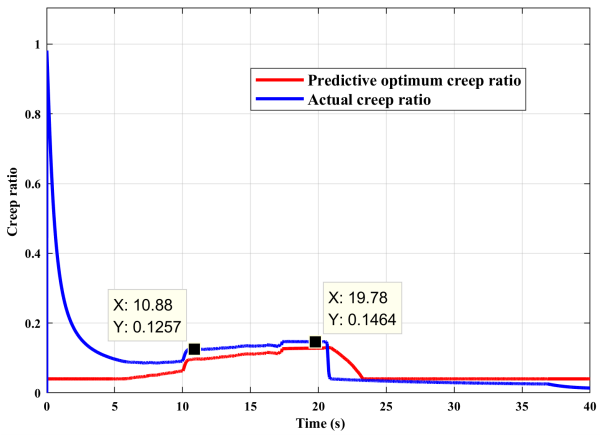

Fig. 16. Creep ratio performance based on torque correction method

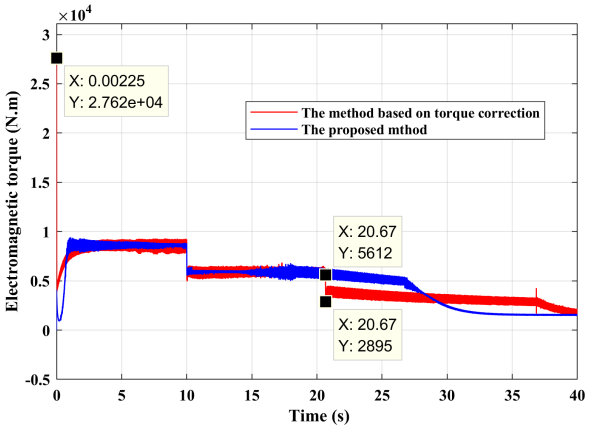

Fig. 17. IPMSM electromagnetic torque performance with comparative simulation

Comparative simulation results show that the proposed method has a higher adhesion utilization and better anti-slip control performance in the traction phase, especially in the start-up phase and in the weak magnetic region of the IPMSM.

4.3. HIL platform test results

In this section, the electric train dynamic model and a wheel-rail model are built based on the starHIL semi-physical simulation platform to enhance the simulation resemblance to actual working conditions. The control method compiled by Simulink has been downloaded directly into the real-time rapid control prototype hardware via rapid prototyping control technology, as shown in Fig. 18. The parameters of train system and controller are consistent with the pure simulation conditions, although the hardware limits the sampling frequency to 10 kHz. Table 4 in the revised manuscript shows the computational burden of two methods (PI method and proposed method). nThe proposed PB-ESO with optimized gains). The memory usage of the proposed method is only 3% higher than PI.

Figure 19 shows the train traction motor speed tracking curves for the proposed and the comparison methods. Figure 20 shows the adhesion coefficients between the wheels and the rails for both methods. Similar to the simulation results, the proposed method has a higher average adhesion utilization in the HIL platform, especially in the high-speed motor operation region. However, during the start-up phase, the adhesion coefficient decreases compared to the simulation results, showing significant fluctuations and even negative values. We analyzed that this is due to the limitation imposed by the hardware computation frequency.

Figure 21 shows the control performance of the motor output torque. Similar to the simulation results, the torque correction method torque performance demonstrates a rapid surge in starting torque, reaching up to $2.8e^{-4}$ Nm. In contrast, the proposed method gradually increases the output torque, providing superior traction control to prevent wheel slip during the start-up phase. However, the proposed method encounters an elevation in dynamic torque pulses due to the limitations imposed by sampling and computation frequencies. As a result, further improvements are required to refine the proposed approach and enhance its adaptability to lower control frequencies in real-world operating conditions.

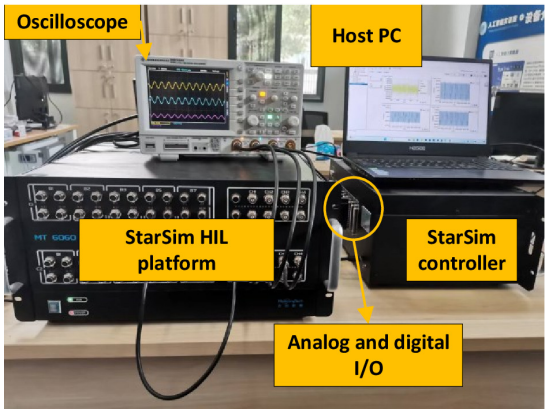

(a)

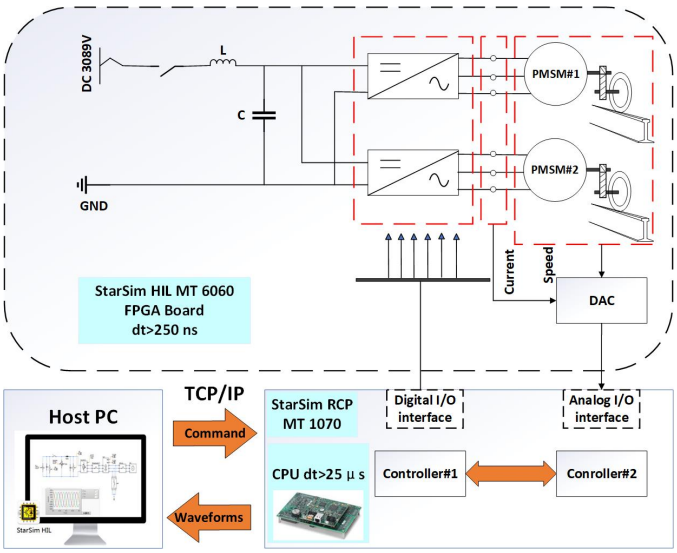

(b)

Fig. 18. Hardware-in-the-loop platform diagram: (a) HIL platform setup; (b) topology of the HIL platform

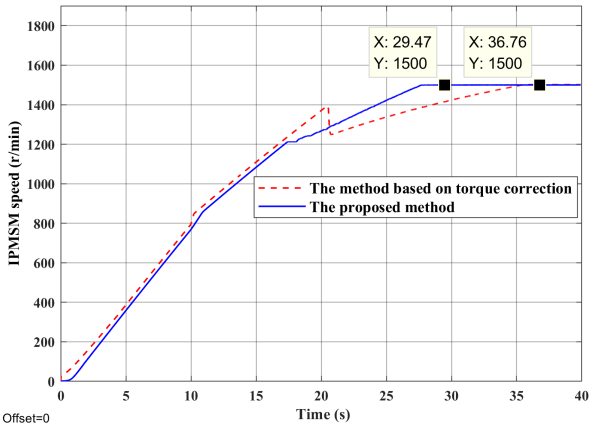

Fig. 19. IPMSM speed tracking performance in the HIL platform

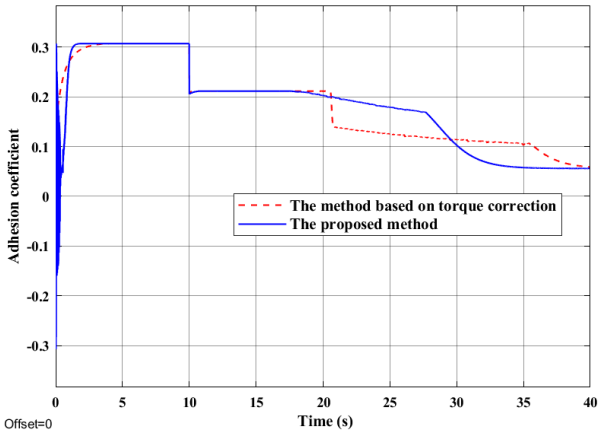

Fig. 20. Adhesion coefficient tracking performance in the HIL platform

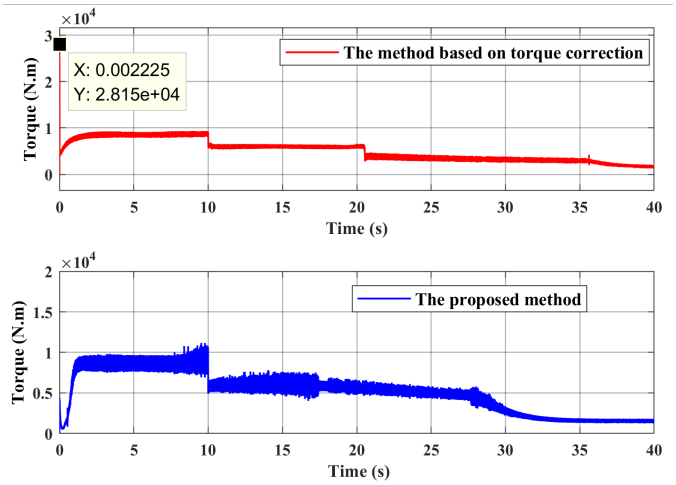

Fig. 21. IPMSM output torque performance in the HIL platform

5. CONCLUSIONS

This study suggests a cascade-free predictive adhesion control technology for IPMSM-driven electric trains, aimed at achieving maximum acceleration. The simulation and HIL platform test results show that the proposed method improves the wheel-rail adhesion utilization during the acceleration phase of the train and obtain superior dynamic performance. In particular, it addresses the issue of excessive start-up torque that can lead to wheel slip with conventional control methods. In addition, the torque performance of the train in the high-speed weak magnetic area of the IPMSM is ensured, enabling the train to attain better tractive effort in this phase.

The proposed control method is still in the laboratory stage. A limitation is that the control performance of the proposed strategy relies heavily on the controller's sampling and calculation frequency. Lower controller calculation frequencies will result in high harmonic torque in the dynamic stage. One can hopefully further enhance the overall control performance of the proposed strategy by improving the optimal slip velocity estimation algorithm and traction motor control algorithms.

APPENDIX

F_{lump} is a non-negative lumped function that measures how far each expected electrical state of the IPMSM is from the desired values. The design details of F_{lump} is as follows

$$F_{\text{lump}} = \underbrace{\gamma_{\text{MTPA}} C_{\text{MTPA}}(k+1)}_{a} + \underbrace{\gamma_{Te} C_{Te}(k+1)}_{b} + \underbrace{\gamma_{I_m} C_{I_m}(k+1)}_{c}, \tag{28}$$

where γ_{MTPA}, γ_{Te}, γ_{I_m} are weighting factors, and we have the following.

- Term (b) is used to achieve the maximum-torque-per-ampere (MTPA) control. The MTPA trajectory is derived by the Lagrange multiplier method and can be described by the formula

$$i_{d\_\text{MTPA}} = \frac{\psi_f}{2(L_q - L_d)} - \sqrt{\frac{\psi_f^2}{4(L_q - L_d)^2} + i_q^2}. \tag{29}$$

  Thus, the form of $C_{Te}(k+1)$ is

$$C_{\text{MTPA}}(k+1) = (i_d(k+1) - i_{d\_\text{MTPA}}(k+1))^2. \tag{30}$$

- Term (b) weights T_{ef} which are high-pass filtered versions of the predictive torque. This penalizes the switching states that generate high frequencies in the predictive torque. As a consequence, the form of $C_{Te}(k+1)$ is

$$C_{Te}(k+1) = (T_{ef}(k+1))^2. \tag{31}$$

- Term (c) is the stator current protection term. It is designed as a nonlinear function,

$$C_{I_m}(k+1) = \begin{cases} \infty, & \sqrt{i_{sd}^2(k+1) + i_{sq}^2(k+1)} \geq I_{\text{lim}}, \\ 0, & \text{else}, \end{cases} \tag{32}$$

  where I_{lim} is the maximum allowable current.

REFERENCES

[1] H. Chen *et al.*, "Wheel slip/slide and low adhesion caused by fallen leaves," *Wear*, vol. 446, p. 203187, 2020.

[2] F. Trimpe and C. Salander, "Wheel–rail adhesion during torsional vibration of driven railway wheelsets," *Veh. Syst. Dyn.*, vol. 59, no. 5, pp. 785–799, 2021.

[3] Y. Zhao and B. Liang, "Re-adhesion control for a railway single wheelset test rig based on the behaviour of the traction motor," *Veh. Syst. Dyn.*, vol. 51, no. 8, pp. 1173–1185, 2013.

[4] G. Wu, L. Shen, and Y. Yao, "Investigating the re-adhesion performance of locomotives with bogie frame suspension driving system," *Int. J. Rail Transp.*, pp. 1–22, 2022.

[5] T. Ishrat, "Slip control for trains using induction motor drive," Ph.D. dissertation, Queensland University of Technology, 2020.

[6] S.D. Chaudhari, P.D. Shendge, and S.B. Phadke, "Dynamic nonlinear gradient observer based extremum seeking control for optimum braking," *IEEE Trans. Ind. Electron.*, vol. 69, no. 3, pp. 2833–2842, 2021.

[7] L. Diao, L. Zhao, Z. Jin, L. Wang, and S.M. Sharkh, "Taking traction control to task: High-adhesion-point tracking based on a disturbance observer in railway vehicles," *IEEE Ind.l Electron. Mag.*, vol. 11, no. 1, pp. 51–62, 2017.

[8] S. Sadr, D.A. Khaburi, and J. Rodríguez, "Predictive slip control for electrical trains," *IEEE Trans. Ind. Electron.*, vol. 63, no. 6, pp. 3446–3457, 2016.

[9] Y. Chen, H. Dong, J. Lü, X. Sun, and L. Guo, "A super-twisting-like algorithm and its application to train operation control with optimal utilization of adhesion force," *IEEE Trans. Intell. Transp. Syst.*, vol. 17, no. 11, pp. 3035–3044, 2016.

[10] M.A. Cimen, Ö. Ararat, and M.T. Söylemez, "A new adaptive slip-slide control system for railway vehicles," *Mech. Syst. Signal Process.*, vol. 111, pp. 265–284, 2018.

[11] K. Nam, S. Oh, H. Fujimoto, and Y. Hori, "Estimation of sideslip and roll angles of electric vehicles using lateral tire force sensors through RLS and Kalman filter approaches," *IEEE Trans. Ind. Electron.*, vol. 60, no. 3, pp. 988–1000, 2012.

[12] P. Pichlik and J. Zdenek, "Locomotive wheel slip control method based on an unscented kalman filter," *IEEE Trans. Veh. Technol.*, vol. 67, no. 7, pp. 5730–5739, 2018.

[13] S. Shrestha, M. Spiryagin, and Q. Wu, "Experimental prototyping of the adhesion braking control system design concept for a mechatronic bogie," *Railway Eng. Sci.*, vol. 29, pp. 15–29, 2021.

[14] T. Hsiao, "Robust estimation and control of tire traction forces," *IEEE Trans. Veh. Technol.*, vol. 62, no. 3, pp. 1378–1383, 2012.

[15] S.H. Park, J.S. Kim, J.J. Choi, and H.-O. Yamazaki, "Modeling and control of adhesion force in railway rolling stocks," *IEEE Control Syst. Mag.*, vol. 28, no. 5, pp. 44–58, 2008.

[16] B. Moaveni, F. Rashidi Fathabadi, and A. Molavi, "Fuzzy control system design for wheel slip prevention and tracking of desired speed profile in electric trains," *Asian J. Control*, vol. 24, no. 1, pp. 388–400, 2022.

[17] P. Pichlik and J. Bauer, "Analysis of the locomotive wheel slip controller operation during low velocity," *IEEE Trans. Intell. Transp. Syst.*, vol. 22, no. 3, pp. 1543–1552, 2020.

[18] N.V. Vantagodi *et al.*, "Design of a scaled roller-rig test bench for anti-slip control development for railway traction," *IEEE Trans. Veh. Technol.*, vol. 72, no. 4, pp. 4320–4331, 2023.

[19] C. Calleja, A. López-de Heredia, H. Gaztañaga, L. Aldasoro, and T. Nieva, "Validation of a modified direct-self-control strategy for PMSM in railway-traction applications," *IEEE Trans. Ind. Electron.*, vol. 63, no. 8, pp. 5143–5155, 2016.

[20] D. Ronanki, S.A. Singh, and S.S. Williamson, "Comprehensive topological overview of rolling stock architectures and recent trends in electric railway traction systems," *IEEE Trans. Transp. Electrif.*, vol. 3, no. 3, pp. 724–738, 2017.

[21] E.J. Fuentes, C.A. Silva, and J.I. Yuz, "Predictive speed control of a two-mass system driven by a permanent magnet synchronous motor," *IEEE Trans. Ind. Electron.*, vol. 59, no. 7, pp. 2840–2848, 2011.

[22] E. Fuentes, D. Kalise, J. Rodriguez, and R.M. Kennel, "Cascade-free predictive speed control for electrical drives," *IEEE Trans. Ind. Electron.*, vol. 61, no. 5, pp. 2176–2184, 2013.

[23] S. Lin, X. Fang, X. Wang, Z. Yang, and F. Lin, "Multiobjective model predictive current control method of permanent magnet synchronous traction motors with multiple current bounds in railway application," *IEEE Trans. Ind. Electron.*, vol. 69, no. 12, pp. 12 348–12 357, 2021.

[24] Y. Zuo, X. Ge, Y. Zheng, Y. Chen, H. Wang, and A. T. Woldegiorgis, "An adaptive active disturbance rejection control strategy for speed-sensorless induction motor drives," *IEEE Trans. Transp. Electrif.*, vol. 8, no. 3, pp. 3336–3348, 2022.

[25] X. Zhang and Y. He, "Direct voltage-selection based model predictive direct speed control for PMSM drives without weighting factor," *IEEE Trans. Power Electron.*, vol. 34, no. 8, pp. 7838–7851, 2018.

[26] C. Mi, H. Lin, and Y. Zhang, "Iterative learning control of antilock braking of electric and hybrid vehicles," *IEEE Trans. Veh. Technol.*, vol. 54, no. 2, pp. 486–494, 2005.

[27] D. Huang, W. Yang, T. Huang, N. Qin, Y. Chen, and Y. Tan, "Iterative learning operation control of high-speed trains with adhesion dynamics," *IEEE Trans. Control Syst. Technol.*, vol. 29, no. 6, pp. 2598–2608, 2021.

[28] J. Lemmens, P. Vanassche, and J. Driesen, "PMSM drive current and voltage limiting as a constraint optimal control problem," *IEEE J. Emerg. Sel. Top. Power Electron.*, vol. 3, no. 2, pp. 326–338, 2015.

[29] M. Alzayed and H. Chaoui, "Efficient simplified current sensorless dynamic direct voltage MTPA of interior PMSM for electric vehicles operation," *IEEE Trans. Veh. Technol.*, vol. 71, no. 12, pp. 12 701–12 710, 2022.

[30] M. Klomp, Y. Gao, and F. Bruzelius, "Longitudinal velocity and road slope estimation in hybrid electric vehicles employing early detection of excessive wheel slip," *Veh. Syst. Dyn.*, vol. 52, no. sup1, pp. 172–188, 2014.

[31] Z. Wang, G. Yu, B. Zhou, P. Wang, and X. Wu, "A train positioning method based-on vision and millimeter-wave radar data fusion," *IEEE Trans. Intell. Transp. Syst.*, vol. 23, no. 5, pp. 4603–4613, 2021.

[32] K. Ko, W. Ahn, and W. Shin, "High-speed train positioning using deep Kalman filter with 5G NR signals," *IEEE Trans. Intell. Transp. Syst.*, vol. 23, no. 9, pp. 15 993–16 004, 2022.

[33] J. Otegui, A. Bahillo, I. Lopetegi, and L.E. Díez, "Evaluation of experimental GNSS and 10-DOF MEMS IMU measurements for train positioning," *IEEE Trans. Instrum. Meas.*, vol. 68, no. 1, pp. 269–279, 2018.

[34] X. Xu, J. Sun, C. Yan, and J. Zhao, "Predictive speed control of interior permanent magnet synchronous motor with maximum torque per ampere control strategy," in *2017 36th Chinese Control Conference (CCC)*. IEEE, 2017, pp. 4847–4852.

[35] Q. Zhang, H. Yu, X. Su, and Y. Li, "Energy consumption analysis of high-speed trains under real vehicle test conditions," *J. Adv. Transp.*, vol. 2022, no. 1, p. 1876579, 2022.

[36] M. Burckhardt, *Fahrwerktechnik: Radschlupf-Regelsysteme*. Vogel, 1993.